CONCLUSION

The newly designed ECAT EXACT HR$^+$ scanner provides an excellent spatial resolution, which can advantageously be used for brain, heart and small animal studies. Whereas the relatively low slice sensitivity may hamper the capability for performing fast dynamic studies in the two-dimensional mode (e.g., $H_2[^{15}O]$ studies), the scanner offers a sufficient sensitivity and count rate capacity for fully three-dimensional whole-body imaging.

ACKNOWLEDGMENTS

REFERENCES

1. Karp JS, Daube-Witherspoon ME, Hoffman EJ, et al. Performance standards in positron emission tomography. *J Nucl Med* 1991;12:2342-2350.
2. *NEMA Standards Publication NU 2-1994*. National Electrical Manufacturers Association, 1994.
3. Kinahan P, Rogers JG. Analytical three-dimensional image reconstruction using all detected events. *IEEE Trans Nucl Sci* 1989;36:964-968.
4. Casey ME, Gadagkar H, Newport D. A component-based method for normalization in volume PET. In: *Proceedings of the 1995 International Meeting on Fully Three-Dimensional Image Reconstruction in Radiology and Nuclear Medicine* 1995:61-65.
5. Bergström M, Eriksson L, Bohm C, Blomqvist G, Litton J. Correction for scattered radiation in a ring detector positron camera by integral transformation of the projections. *J Comput Assist Tomogr* 1983;7:42-50.
6. Hoverath H, Kuebler WK, Ostertag HJ, et al. Scatter correction in the transaxial slices of a whole-body positron emission tomograph. *Phys Med Biol* 1993;38:717-728.
7. Watson CC, Newport D, Casey ME. A single scatter simulation technique for scatter correction in three-dimensional PET. In: Grangeat P, Amans JL, eds. *Three-dimensional image reconstruction in radiology and nuclear medicine.* Dordrecht, The Netherlands: Kluwer; 1996:255-268.
8. Karp JS, Muehllehner G. Standards for performance measurements of PET scanners: evaluation with the UGM PENN-PET 240H scanner. *Med Prog Technol* 1991;17:173-187.
9. Bice AN, Miyaoka RS. Standardized tests of PET performance. *J Nucl Med* 1992;33:1429-1430.
10. Wienhard K, Dahlbom M, Eriksson L, et al. The ECAT EXCAT HR$^+$ performance of a new high resolution positron scanner. *J Comput Assist Tomogr* 1994;18:110-118.
11. DeGrado TR, Turkington TG, Williams JJ, Stearns CW, Hoffmann JM, Coleman RE. Performance characteristics of a whole-body PET scanner. *J Nucl Med* 1994;35:1398-1406.
12. Adam LE, Zaers J, Ostertag H, et al. Performance evaluation of the PET scanner ECAT EXACT HR$^+$. In: Karp J, ed. *IEEE 1996 NSS and MIC Conference Record*; in press.
13. Rota Kops E, Herzog H, Schmid A, Holte S, Feinedegen LE. Performance characteristics of an eight ring whole body PET scanner. *J Comput Assist Tomogr* 1990;14:437-445.
14. Wienhard K, Eriksson L, Groontoonk S, Casey M, Pietrzyk U, Heiss WD. Performance evaluation of the positron scanner ECAT EXACT. *J Comput Assist Tomogr* 1992;16:804-813.
15. Townsend DW, Wensveen M, Byars LG, et al. A rotating PET scanner using BGO block detectors: design, performance and applications. *J Nucl Med* 1993;34:1367-1376.
16. Moses WW, Derenzo SE. Empirical observation of resolution degradation in positron emission tomographs utilizing block detectors. *J Nucl Med* 1993;34:101P.
17. Cherry SR, Dahlbom M, Hoffmann EJ. Three-dimensional PET using a conventional multislice tomograph without septa. *J Comput Assist Tomogr* 1991;15:655-668.

Improved Resolution for PET Volume Imaging through Three-Dimensional Iterative Reconstruction

Jeih-San Liow, Stephen C. Strother, Kelly Rehm and David. A. Rottenberg

PET Imaging, Veterans Administration Medical Center; Departments of Radiology and Neurology, University of Minnesota, Minneapolis, Minnesota

It has been demonstrated that in two-dimensional iterative reconstruction, a resolution model can improve image resolution while controlling noise. With the lower noise levels of three-dimensional PET volume imaging, these iterative reconstruction advantages may be extended to three dimensions to further improve the reconstructed image resolution. **Methods:** We have implemented three-dimensional versions of iterative filtered backprojection (IFBP) and the maximum likelihood by expectation maximization (ML-EM) reconstruction algorithms and applied them to three-dimensional PET volume datasets. The results were compared to images obtained using the standard three-dimensional reprojection reconstruction (3DRP) algorithm. **Results:** For IFBP with 15 iterations and no regularization compared to 3DRP, both using a ramp filter, the transaxial resolution improved 52%, and the axial resolution improved 39%. With a strong regularization, the transaxial and axial resolution improvements were reduced to 6% and 5%, respectively. If a Hanning roll-off is applied to the ramp filter in the transaxial direction, the transaxial resolution for IFBP without regularization improved 35% compared to 3DRP; with regularization the improvement dropped to 19%. The axial resolution for IFBP and 3DRP was unaffected by this transaxial smoothing in the reconstruction filter. With the same Hanning roll-off, the noise for IFBP without regularization increased by a factor of 6 compared to 3DRP; with regularization the noise was increased only by a factor of 3. Compared to IFBP, the three-dimensional ML-EM reconstruction produced similar resolution improvements with a much smaller increase in noise and slower convergence. Resolution improvements from both IFBP and ML-EM reconstructions are visually apparent in three-dimensional FDG brain images and result in increased activation signals in a three-dimensional [^{15}O]water functional activation study. **Conclusion:** Our results demonstrate that resolution improvement is possible for IFBP and ML-EM compared to 3DRP with or without noise increase.

Key Words: PET; three-dimensional volume imaging; iterative reconstruction; resolution improvement

J Nucl Med 1997; 38:1623-1631

The removal of interplane septa to allow off-plane coincidences to be collected for multi-ring detectors has increased the sensitivity of PET cameras (*1,2*). This increased sensitivity is especially useful in studies where the required frame duration is short, the tracer used has a short half-life, or the tracer uptake is limited and confined to small regions within the scanning field of view (*3*). However, there are two drawbacks to three-dimensional PET volume imaging (PVI). First, the oblique penetration of photons in the detectors degrades the axial resolution compared with two-dimensional imaging with the septa extended (*3,4*). Second, the standard three-dimensional filtered backprojection reconstruction (the three-dimensional reprojection algorithm (3DRP) (*5*)) is based on forward projecting a low-statistics two-dimensional image volume to estimate the missing part of the truncated projections, followed by a full

three-dimensional filtered backprojection. As a result, reconstructed images contain a significant amount of estimated data in the end planes, which degrades the transaxial resolution in the end planes relative to the central planes (3). Other three-dimensional reconstruction methods such as FAVOR (6) or pseudo three-dimensional methods using rebinning approaches [e.g., single-slice rebinning (7), multislice rebinning (8) and frequency-space rebinning (9)] were proposed primarily to avoid the manipulation of large datasets and the computational burden of the full three-dimensional forward- and backprojection in 3DRP. These alternative three-dimensional reconstruction methods may be suitable for some imaging situations [e.g., small axial acceptance angle (10)], but they do not attempt to recover the lost axial resolution, and they are not expected to have better noise performance than 3DRP.

Iterative reconstruction algorithms have been extensively studied in two-dimensional imaging. Their ability to incorporate models such as resolution, attenuation and scatter during the reconstruction process can, in general, improve reconstructed image quality compared to filtered backprojection (FBP). Among two-dimensional iterative algorithms, iterative filtered backprojection (IFBP) was initially developed to handle missing projections for CT reconstruction (11) or to estimate and compensate for attenuation in SPECT imaging (12). As a general reconstruction algorithm, the two major advantages of IFBP over most other iterative algebraic methods are its relatively fast convergence due to the use of a filtered back-projector (13) and its ease of implementation. Because IFBP uses the filtered backprojection operator in the standard filtered backprojection reconstruction, one needs only to implement the forward projector. For three-dimensional IFBP, it is even easier since the algorithm can be directly modified from 3DRP, which uses both a three-dimensional forward projection and a three-dimensional filtered backprojection operator. Another widely studied iterative reconstruction algorithm, Maximum Likelihood by Expectation Maximization (ML-EM), is based on a Poisson noise model coupled with an inherent positivity constraint (14,15). In two dimensions, ML-EM images have proven to have some noise advantage over both FBP and IFBP images if resolution recovery beyond the intrinsic detector resolution is desired (16) or if low-count areas are compared (17). However, the major problem with ML-EM is its slow convergence, which is expected to become even worse in three dimensions as the size of the dataset increases significantly compared to that in two dimensions.

Recently, several modified iterative reconstruction algorithms have been proposed. Some have focused on speeding up convergence (18,19), while others have tried to improve signal-to-noise ratios by introducing penalties (20) or side information (21). However, most of these methods have been tested only with simple simulations or limited real data, and additional investigations are required to demonstrate their practical performance. In addition, many of these methods, which are complicated and require significant computer resources when implemented in two dimensions, are presently computationally impractical in three dimensions. The goal of this paper is not to select the best or the fastest iterative reconstruction algorithm for PVI. Rather, we demonstrate the comparatively simple, direct extension of two-dimensional IFBP and ML-EM (in their original forms) into three dimensions and investigate whether their advantages for two-dimensional studies carry over into three-dimensional studies. In particular, the sensitivity increase due to three-dimensional acquisition for PVI may be used to obtain improved three-dimensional resolution for the same noise levels obtained with the two-dimensional algorithms,

such as an improved signal-to-noise ratio. Preliminary results of resolution and noise measurements for three-dimensional IFBP and ML-EM are compared to those from 3DRP based on-line sources and a 20-cm cylindrical phantom. Applications to FDG and [^{15}O]water studies of the human brain are given. The reconstruction time using the two iterative algorithms implemented in three dimensions is also discussed.

THEORY

Iterative Filtered Backprojection

Iterative filtered backprojection belongs to one of the iterative algebraic reconstruction methods. The generalized process of iterative algebraic reconstruction can be expressed by the following equation (13):

$$x^{(k+1)} = x^{(k)} + rO(p - Ax^{(k)}), \qquad \text{Eq. 1}$$

where $x^{(k+1)}$ and $x^{(k)}$ denote the image vector at the $(k+1)$th and kth iteration, A is the system transition matrix mapping the object from image space to projection space, p is the measured projections, r is an overrelaxation parameter and O is a generalized backprojection operator. For IFBP, O is replaced by a filter followed by a backprojector, the same operation normally performed in FBP. Instead of converging to the least-squares solution, IFBP converges to a weighted least-squares solution with the reconstruction filter being the weighting function (13,22). If only a ramp filter is used, the algorithm is equivalent to weighting by an ideal delta point-spread response (PSR). In two-dimensional cases, a similar situation occurs with a preconditioning filter (23) derived from a simulated two-dimensional PSR, but the preconditioning filtering operates in two-dimensional space after the backprojection operation, whereas the IFBP approach applies a one-dimensional filter to the projections before the backprojection. A smoothing roll-off applied to the ramp filter for noise reduction in IFBP is similar to a penalty function. Depending on how O is chosen, Equation 1 also may become ART, SIRT, Landweber, Generalized Landweber or weighted least-squares. A detailed discussion on this iterative algebraic reconstruction framework and its convergence properties is given in (13).

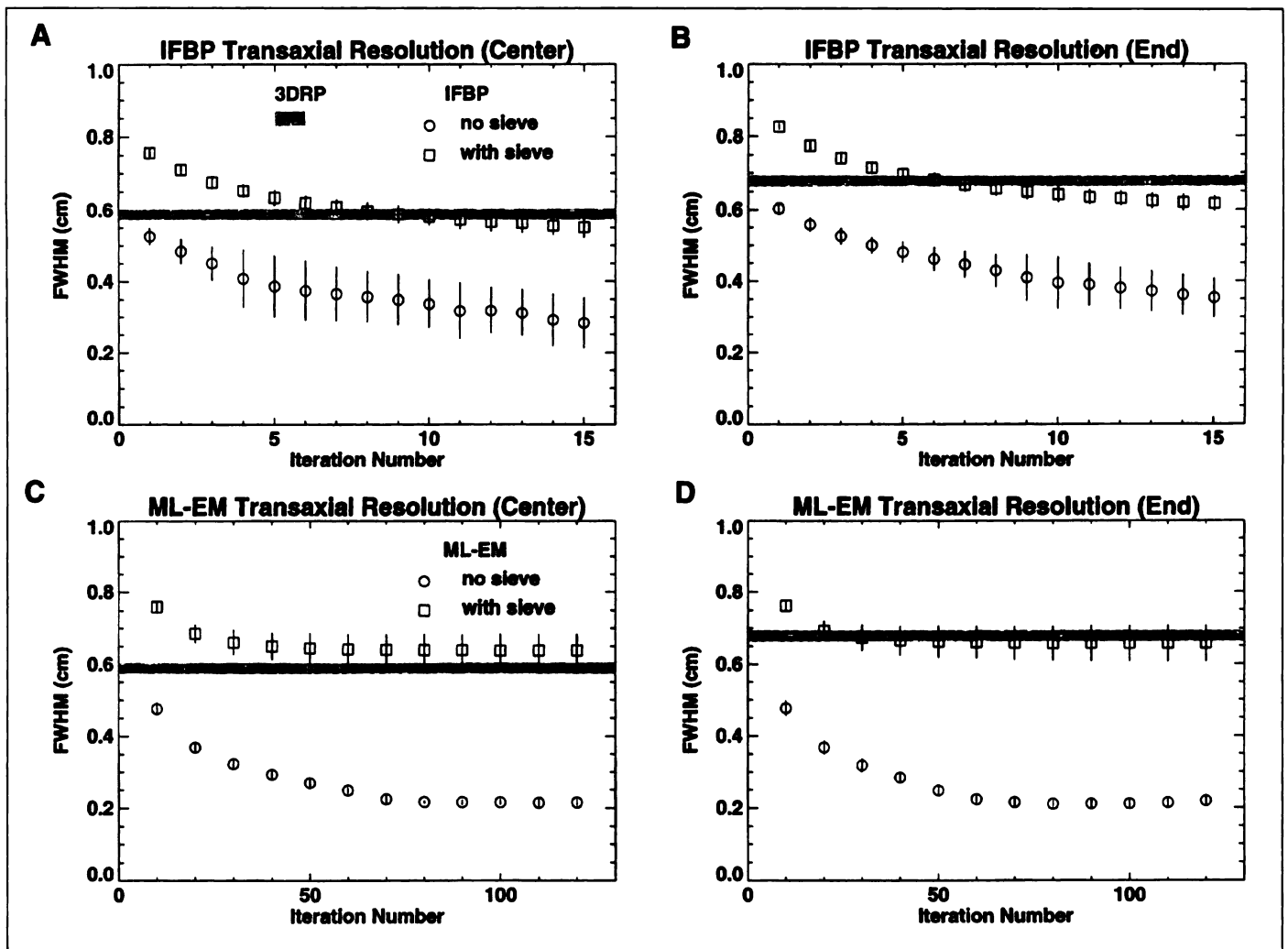### Maximum Likelihood by Expectation Maximization (ML-EM)

The basic working equation for an ML-EM algorithm based on maximizing the log-likelihood function of a Poisson distribution is:

$$x_i^{k+1} = x_i^k \left[\sum_j a_{ij}(p_j/p_j') \right] / \sum_j a_{ij} \qquad \text{Eq. 2}$$

where

$$p_j' = \sum_i a_{ij}x_i^k$$

i and j are the indices of image pixel and projection sample, respectively. p_j is the measured projection, p_j' is the calculated forward projection and a_{ij} is the system transition matrix, the elements of A in IFBP (Eq. 1). x_i^{k+1} and x_i^k are the image pixel values at the $(k+1)$th and kth iterations. It is well established that as the IFBP and ML-EM solutions converge, they become very noisy and require some form of regularization for the images to be useful. In this study, we chose to apply the method of sieves (24) in the form of a postreconstruction filter for regularization noise control.

FIGURE 1. (A,B) Mean transaxial resolution measured from sources at the axial center (Plane 16) and the axial end (Plane 30) for iterative filtered backprojection (IFBP) and (C,D) maximum likelihood by expectation maximization (ML-EM) compared to three-dimensional reprojection (3DRP, horizontal line). The bars on each symbol and the thickness of the shaded line represent the standard deviation of the mean resolution of the five sources. For 3DRP and IFBP, no smoothing was applied in the reconstruction filter. For IFBP and ML-EM, a three-dimensional Gaussian of FWHM 0.58 × 0.58 × 0.5 cm was used as both the resolution and the sieve kernel.

MATERIALS AND METHODS

All experiments and measurements were conducted on a Siemens ECAT 953B PET camera (Knoxville, TN) with an axial field of view of 10.8 cm (2). Data were reconstructed into contiguous two-dimensional image volumes consisting of 31 slices. A measured attenuation correction was performed based on two-dimensional transmission scans.

Spatial Resolution and Noise

To obtain a set of three-dimensional resolution measurements for the 953B camera, the following experiments were conducted. For transaxial resolution, five sources made of capillary tubes of 0.08/0.11 mm (ID/OD) × 90 mm containing high concentrations of ^{18}F were aligned parallel to the axial direction on a rigid frame and separated by 4 cm from each other radially (25). Static emission scans were acquired in three-dimensional mode at two different axial locations: axial center (Plane 16) and one axial end (Plane 30). For axial resolution, three capillary tubes filled with ^{18}F were attached to the frame perpendicular to the axial direction and separated from each other by 8 cm radially. Data were collected only for the axial center (Plane 16). To improve axial sampling for the axial resolution measurement, 10 three-dimensional static emission scans were acquired with axial offsets of 0.1 cm with respect to each other. All images were reconstructed by 3DRP, IFBP up to 15 iterations and ML-EM up to 120 iterations with no

attenuation correction. For IFBP and ML-EM, a spatially invariant three-dimensional Gaussian function approximating the measured PSR of the camera was used as the resolution model (FWHM = 0.58 × 0.58 × 0.5 cm). To mimic real scanning situations where noise is present, the same three-dimensional Gaussian function was also used as the postreconstruction sieve filter for regularization. For 3DRP and IFBP, two different reconstruction filters were used: (a) a ramp filter with no smoothing, representing the ideal (noiseless) condition for maximum resolution recovery and (b) the same ramp filter with Hanning roll-off to the Nyquist frequency (1.6 cycles/cm) only in the transaxial direction. The FWHM of the transaxial resolution was obtained by fitting a one-dimensional Gaussian function to each source transaxially in the reconstructed images. The FWHM of the axial resolution was obtained by fitting a Gaussian to the axial samples extracted from the 10 reconstructed images with 0.1-cm spacing about each source.

To measure the image noise associated with each reconstruction algorithm, a separate three-dimensional scan of a 20-cm solid cylindrical germanium phantom was acquired. Images were reconstructed by 3DRP, IFBP up to 15 iterations and ML-EM up to 120 iterations. The 15-iteration stopping point for IFBP was chosen based on our previous two-dimensional experience (13), and the 120-iteration stopping point for ML-EM was chosen because of the asymptotic behavior of its image resolution (Fig. 1). Corrections
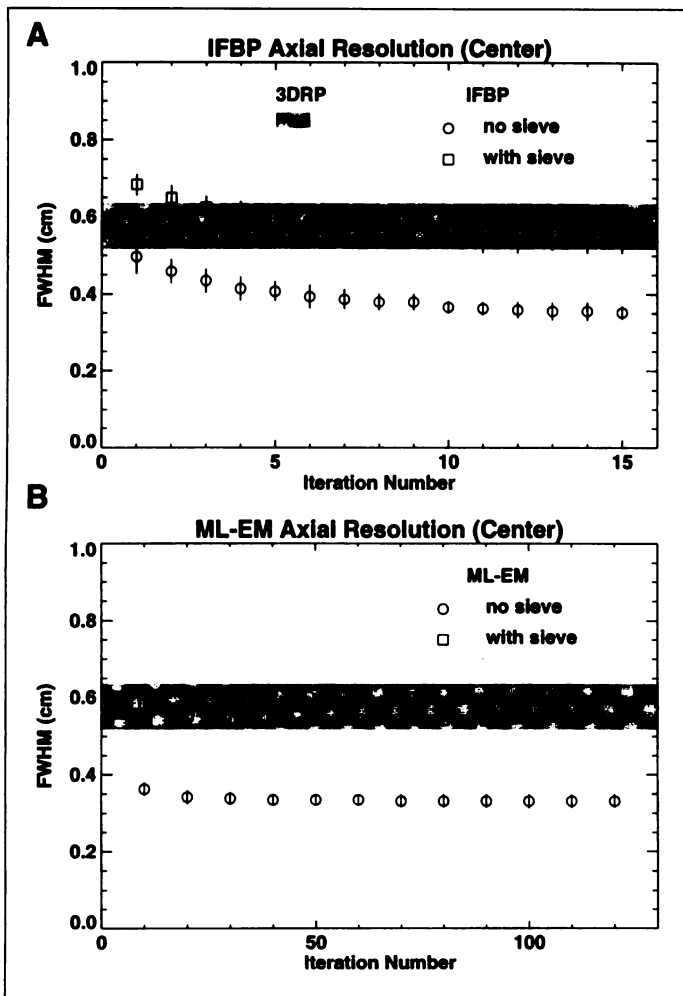
FIGURE 2. (A) Mean axial resolution measured from sources at the axial center for IFBP and (B) ML-EM compared to 3DRP (horizontal line). For 3DRP and IFBP, no smoothing was applied in the reconstruction filter. For IFBP and ML-EM, a three-dimensional Gaussian of FWHM 0.58 × 0.58 × 0.5 cm was used as both the resolution and the sieve kernel. See Figure 1 for the key to the bars and thickness of the shaded line.

FIGURE 3. Mean transaxial resolution measured from sources at the axial center for IFBP reconstructed with a Hanning roll-off to the Nyquist frequency in the transaxial direction compared to 3DRP (horizontal line). A three-dimensional Gaussian of FWHM 0.58 × 0.58 × 0.5 cm was used as both the resolution and the sieve kernel. See Figure 1 for the key to the bars and thickness of the shaded line.
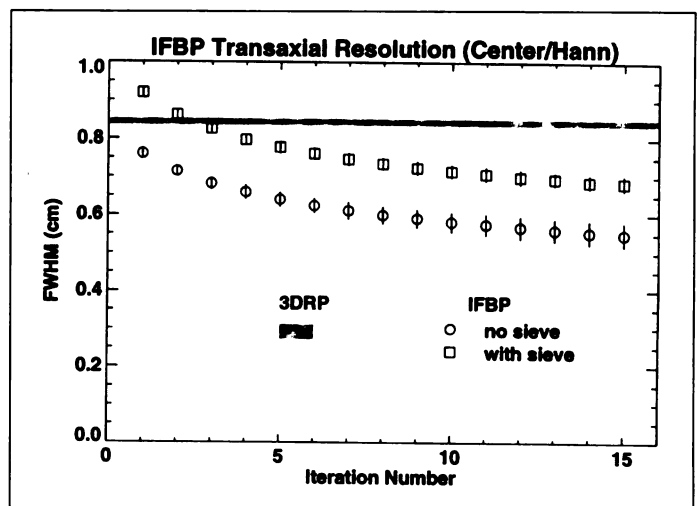
for measured attenuation, randoms and detector homogeneity (normalization) were applied before the reconstruction. For 3DRP and IFBP a ramp filter with Hanning roll-off to the Nyquist frequency in the transaxial direction was used. A mean and standard deviation were measured for each plane using a 15-cm ROI placed at the center of the cylinder, and the results were compared for all three reconstruction algorithms.

FDG Brain Data

A 5-min, three-dimensional FDG scan of a normal human brain was obtained 40–45 min after the injection of 5 mCi FDG. Data were reconstructed by 3DRP, IFBP and ML-EM with the same settings previously described for the cylinder. For 3DRP and IFBP the ramp filter with Hanning roll-off to the Nyquist frequency in the transaxial direction was used. Regularization with the Gaussian sieve was applied to IFBP and ML-EM images. Results from the three reconstructions were compared.

Oxygen-15-Water Brain Activation Study

A total of eight three-dimensional scans were acquired in a functional activation (speech) study. For each scan, approximately 17.5 mCi [^{15}O]water were infused intravenously at 1 ml/sec by means of a computer-controlled infusion system (26). PET scanning commenced when the radioactive tracer reached the brain, typically 10–20 sec after injection (detected by an abrupt increase in total scanner counts), and data acquisition continued for 90 sec.

Scans alternated between baseline (unstimulated) and activated conditions with 10-min rest periods in between to allow for ^{15}O decay. During the four activated scans, the subject was asked to perform a speech task (sounding nonsense syllables). Data were reconstructed by 3DRP and by IFBP up to 15 iterations, both with Hanning roll-off to the Nyquist frequency in the transaxial direction. After aligning the eight volumes with respect to the first (baseline) volume using a six-parameter rigid body transformation (27) and normalizing by administered dose and subject weight, a subtraction analysis was applied (28). Subtraction and t-statistics images were generated for the two reconstructions, respectively, and compared (28).

RESULTS

Spatial Resolution

Figure 1 compares the mean transaxial resolution of the five sources measured from the three reconstructions at two different axial locations. For 3DRP and IFBP, a ramp filter with no roll-off was used. The mean transaxial resolutions of the five sources for IFBP and ML-EM are calculated and plotted as a function of the iteration number. For IFBP with no sieve compared to 3DRP, the mean resolution at all iterations is better and improves as the number of iterations increases. At 15 iterations, the mean transaxial resolution has improved 52% at the center and 48% at the end (Figs. 1A and B). For IFBP with sieve compared to 3DRP, the transaxial resolution is initially worse and becomes better for 10–15 iterations. The mean transaxial resolution improvements at 15 iterations are 6% at the center and 9% at the end. Note that the mean transaxial resolution for 3DRP degrades from 0.6 cm at the center (Fig. 1A) to 0.68 cm at the end (Fig. 1B) because of the forward projection in the reconstruction. For IFBP with sieve at 15 iterations, the transaxial resolutions at the axial center with respect to the radial distance at 8 cm, 4 cm and 0 cm are 0.58 cm, 0.52 cm and 0.54 cm, respectively. This radial difference is about 10% and is slightly smaller at the axial end. On the other hand, 3DRP shows a quite uniform (0.6 cm) resolution regardless of the radial positions. Mean transaxial resolution for ML-EM also improves as the number of iterations increases. For ML-EM at 120 iterations without sieve compared to 3DRP, the mean transaxial resolution improvements at both the axial
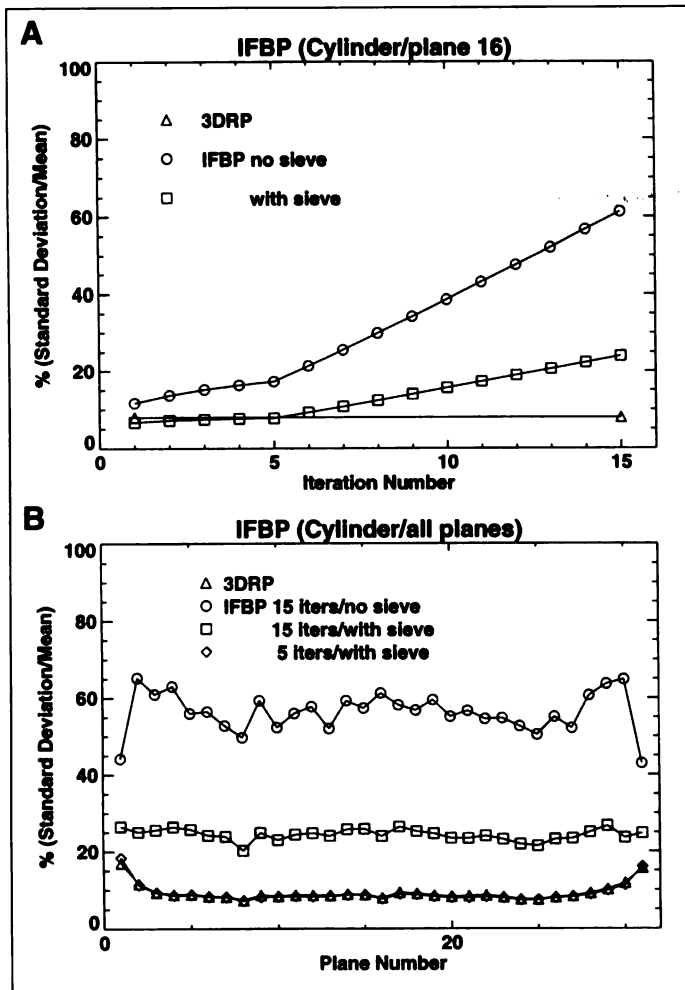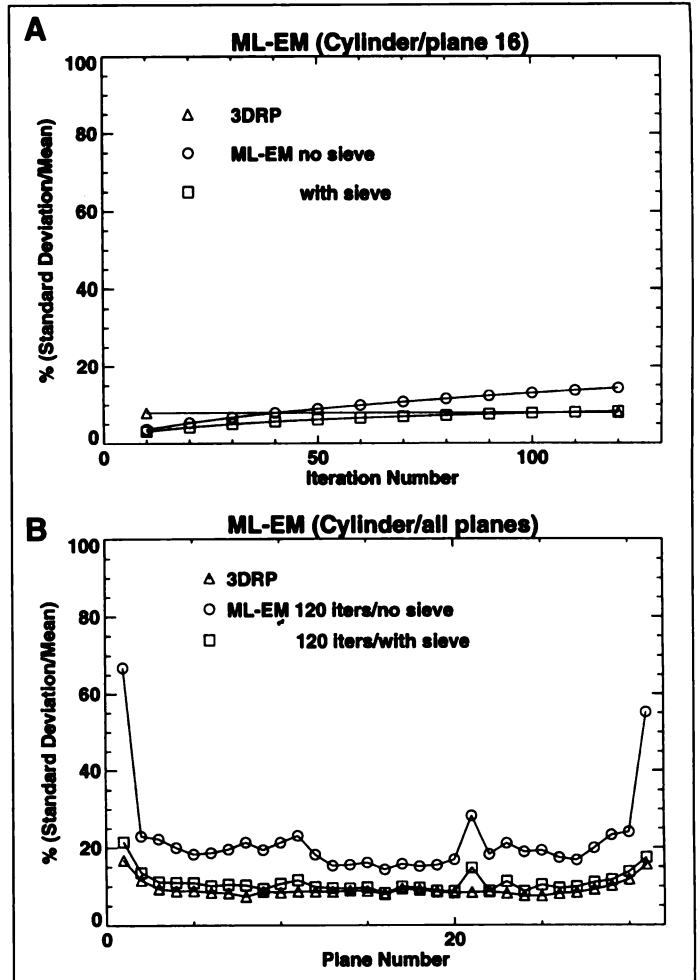
FIGURE 4. (A) Normalized standard deviation (s.d./mean × 100) measured from a 15-cm ROI at the axial center (Plane 16) of a 20-cm cylinder reconstructed by IFBP compared to 3DRP. (B) Normalized standard deviation of the 15-cm ROI for all planes reconstructed by IFBP at 5 and 15 iterations compared to 3DRP. Both 3DRP and IFBP are with a Hanning roll-off to the Nyquist frequency in the transaxial direction.

FIGURE 5. (A) Normalized standard deviation (s.d./mean × 100) measured from a 15-cm ROI at the axial center (Plane 16) of a 20-cm cylinder, reconstructed by ML-EM compared to 3DRP. (B) Normalized standard deviation of the 15-cm ROI for all planes reconstructed by ML-EM at 120 iterations compared to 3DRP. The 3DRP is with a Hanning roll-off to the Nyquist frequency in the transaxial direction.

center and the axial end are >60% (Figs. 1C and D). With sieve regularization, the transaxial resolution at the center becomes slightly worse than that of 3DRP (Fig. 1C). At the axial end, ML-EM with sieve retains a constant slight improvement after 40 iterations compared to 3DRP (Fig. 1D).

Figure 2 compares the mean axial resolution of the three sources measured from the three reconstructions at the axial center. With no sieve, both IFBP at 15 iterations and ML-EM at 120 iterations show mean axial resolution improvements >30%. After sieve, the improvements are reduced to 5%. Note that the axial resolution measured from the three sources for IFBP with sieve and for ML-EM both with and without sieve are more uniform compared to 3DRP. Both the transaxial and axial resolution for ML-EM improves very slowly after 40 iterations (Figs. 1C, D and 2B).

The results in Figures 1 and 2 represent resolution improvements for situations where statistical noise is not a concern. In practice, when Poisson noise is present, additional smoothing is usually necessary to achieve a better signal-to-noise ratio in the reconstructed images. Figure 3 compares the mean transaxial resolution measured from 3DRP and IFBP reconstructions at the axial center, both using a ramp filter with Hanning roll-off to the Nyquist frequency in the transaxial direction. The mean transaxial resolution for 3DRP is degraded to 0.85 cm with the Hanning roll-off. Similar degradation also is observed for IFBP.

However, compared to 3DRP, the transaxial resolution improvement for IFBP with sieve occurs at three iterations instead of at nine iterations, and at 15 iterations there is a 19% improvement compared to the 6% obtained using a ramp filter without roll-off (Figs. 1A and 3). The axial resolution of both 3DRP and IFBP were unaffected by this transaxial smoothing as expected.

Noise

Figure 4A compares the noise indicated by normalized standard deviation (s.d./mean × 100) from a 15-cm ROI centered on images of a 20-cm cylindrical phantom reconstructed by 3DRP and IFBP, both using a ramp filter with Hanning roll-off to the Nyquist frequency in the transaxial direction. For IFBP the noise increases as the number of iterations increases. Compared to 3DRP, the noise for IFBP at 15 iterations with no sieve is seven times higher; with sieve regularization, the noise is reduced but is still higher. Figure 4B illustrates the normalized standard deviation of all planes for 3DRP compared to IFBP at 5 and 15 iterations. At 15 iterations, the noise in most central planes is higher by a factor of 7 without sieve and reduces to a factor of about 3 with sieve. On the other hand, the noise of IFBP at five iterations with sieve is almost the same as in 3DRP. Results of the same mean and standard deviation measurements for ML-EM are shown in Figure 5. The noise for ML-EM at 120 iterations without sieve

TABLE 1
Summary of Key Results in Resolution FWHM and Noise
Comparison for IFBP, ML-EM and 3DRP

	Resolution FWHM (cm)		Noise % (std/mean)	
	Transaxial		Axial	Axial
	Center	End	Center	Center
IFBP (15 iterations)				
Ramp with sieve	0.55	0.62	0.55	
Hann with sieve	0.68		0.53	24.0
(5 iterations)				
Hann with sieve	0.78		0.58	7.7
ML-EM (120 iterations)				
with sieve	0.64	0.66	0.54	8.2
3DRP Ramp	0.59	0.68	0.58	
3DRP Hann	0.84		0.59	7.9

For IFBP and ML-EM, only reconstructions with sieve regularization are shown. The noise was calculated from a 15-cm ROI located on Plane 16 (at the axial center). Numbers that are missing were not measured in this study.

is approximately a factor of 2 higher than that of 3DRP for most except the two end planes. With sieve regularization, the noise is reduced to the level of 3DRP and is quite consistent for all planes (Fig. 5B).

Table 1 summarizes the key results in comparing resolution FWHM and noise for IFBP, ML-EM and 3DRP. The results clearly demonstrate that resolution improvement is possible for IFBP and ML-EM compared to 3DRP with or without noise increase. However, the number of iterations and the Gaussian sieve used for comparison in Table 1 are not necessarily optimal.

FDG Brain Data

Figure 6 compares a three-dimensional human brain FDG volume reconstructed by the three algorithms. The top left panel illustrates images reconstructed by 3DRP. The corresponding IFBP images at five and 15 iterations with sieve regularization are shown at the top right and bottom left, respectively. Images at the bottom right were reconstructed by ML-EM at 120 iterations with sieve regularization. The images of IFBP and ML-EM were selected based on their subjective visual appear-

ance. Therefore, the resolution matching–a crucial factor when comparing quantitative imaging performance (29)–is not considered optimal here. Figure 6 demonstrates that: (a) compared to 3DRP, the resolution improvement for IFBP and ML-EM can be clearly seen in both the transaxial and axial (coronal and sagittal slices) directions; (b) compared to ML-EM at 120 iterations, IFBP at 15 iterations achieves the same or better resolution faster at the price of higher image noise. On the other hand, compared to ML-EM at 120 iterations, IFBP at five iterations achieves slightly less resolution improvement but with images appearing to be visually similar.

Oxygen-15-Water Brain Activation Study

Figure 7 demonstrates the results of an [^{15}O]water speech study reconstructed by 3DRP and IFBP. Only significant activations in the temporal lobes (the two bright areas on the left and right sides of the brain) are illustrated. For purposes of comparison, spheres within the corner-cube environment were used to represent the volumes and centroids of face-connected voxels in the activated foci (30). Cluster size was determined using a 98th percentile threshold from the subtraction image of 3DRP. (The threshold was determined by voxel values above the 98th percentile of the voxel distribution in the 3DRP subtraction images.) An MRI volume of the same subject was registered to both subtraction volumes using the same six-parameter rigid body transformation (27) and displayed on the inner surface of the cube. Compared to 3DRP, the resolution improvement for IFBP is indicated by the larger volume of the activated foci in the subtraction image (Table 2). The volume increase is 41% in the left temporal lobe and 23% in the right temporal lobe, both with a ≈4% increase in mean intensity. The centroid of the two activated areas remained unchanged. The average t values of the two foci for IFBP are smaller compared to 3DRP (Table 2). For both reconstructions, all voxels within the two foci (above the 98th percentile) passed a significance level of p = 0.01. However, for the same voxels, the number of statistically significant voxels for IFBP dropped substantially with a p value threshold of 0.001 compared to 3DRP (Table 2).
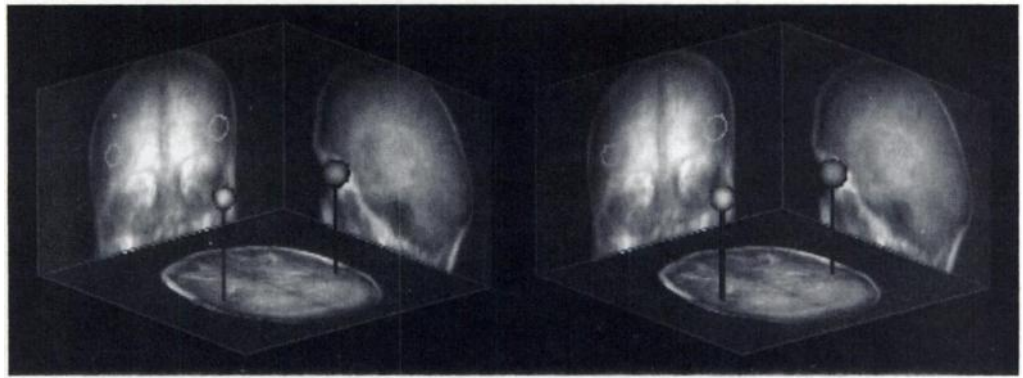
Reconstruction Time

Figure 8 compares the reconstruction time per iteration for three-dimensional IFBP and ML-EM as a function of up to four CSPI's i860-based supercard II array processors (Billerica,
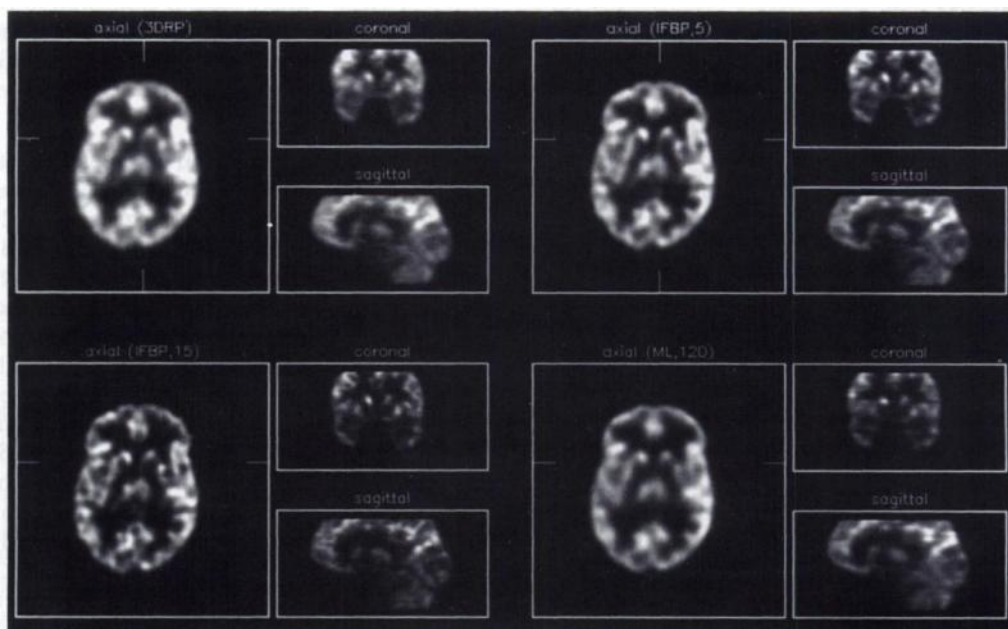
FIGURE 6. A three-dimensional FDG brain volume reconstructed by 3DRP (top left), IFBP at five iterations (top right), IFBP at 15 iterations (bottom left) and ML-EM at 120 iterations (bottom right). Both 3DRP and IFBP are with a Hanning roll-off to the Nyquist frequency in the transaxial direction. All IFBP and ML-EM volumes are regularized with a Gaussian sieve of FWHM 0.58 × 0.58 × 0.5 cm.

FIGURE 7. A corner cube representation of selected activated areas in the temporal lobes due to a speech task. Results are from an [^{15}O]water study reconstructed by 3DRP (left) and from IFBP for 15 iterations with sieve regularization (right). The voxels shown in both images were selected based on a 98th percentile threshold of the subtraction volume of 3DRP. The wallpaper on the sides of the cube are radiograph-style integrations through the MRI dataset of the same subject.

MA) currently available at the Minneapolis VA Medical Center. The average reconstruction time for IFBP is 17 min per iteration for our routine configuration of three supercards on a SUN 4/370 workstation, which is about the same as 3DRP. The reconstruction time for ML-EM per iteration using the same three-supercard configuration is 27 min, 60% more than measured for IFBP. For IFBP, the speedup factors from one to four supercards are 1:1.5:2.3:3.3. The magnitude of the speedup factors from one to three supercards are about the same for ML-EM. The fourth supercard was not available at the time the three-dimensional ML-EM reconstruction was performed.

DISCUSSION

The use of iterative reconstruction algorithms with a resolution model to improve reconstructed image resolution while controlling noise has been studied in many two-dimensional imaging situations. This paper extends two of the widely discussed two-dimensional iterative algorithms into three dimensions and demonstrates that, compared to 3DRP, resolution improvement in both the transaxial and axial directions can be achieved (Figs. 1 and 2). The transaxial resolution improvement can be greater than 48%, such as in the case of IFBP reconstructed with a ramp filter without regularization. With a Hanning roll-off applied to the ramp filter to control noise in the transaxial direction, IFBP with regularization still maintains a 19% transaxial resolution improvement compared to 3DRP (Fig. 3) with up to three times more noise (Fig. 4). However, at 5 iterations IFBP with regularization achieves a 10% transaxial resolution improvement with little noise increase compared to 3DRP (Figs. 3 and 4A). Both the resolution and noise performance of IFBP at 5 and 15 iterations are consistent with the visual appearance of their respective images (Fig. 6). Compared

to 3DRP, the axial resolution for IFBP at 15 iterations with regularization improved by 5% and was unaffected by transaxial smoothing in the reconstruction filter.

The choice of a sieve filter equivalent to the Gaussian PSR results in a reconstructed image resolution approximately equal to the intrinsic detector resolution (24). We used these sieved images to represent the worst-case scenario in our resolution improvement attempt. It is certainly possible to reduce the sieve size, trading noise for resolution recovery, since in PVI the increased sensitivity compared to two-dimensional imaging provides a considerable noise advantage. In addition, many tasks (e.g., typical ROI measurements) will not be applied on images reconstructed using the worst-case voxel-based noise measurements reported here. These trade-offs need to be carefully studied for specific tasks. In the subtraction study for IFBP compared to 3DRP, the volume of activated foci increased together with a slight increase in the mean value for the activated foci. This is exactly what happens in a resolution improvement when the structure is much larger than the resolution FWHM. The process involves sharpening the edges and moving counts from outside to inside the structure, resulting in more voxels above the threshold without a significant mean increase. On the other hand, the t values in the IFBP foci are lower than for 3DRP, as a result of higher noise in the individual IFBP images. Since the voxels are not independent measurements and the two reconstructed images have different resolutions (Fig. 3), their p-value thresholds need to be adjusted accordingly to reflect the same confidence level. Because none of the foci's voxels are significant for either reconstruction with the Bonferroni correction (31) (a very conservative adjustment for data dependency), we compared the effect of two confidence

TABLE 2
Volume Size, Volume Mean, Centroid and t Values of Activated Foci in the Left Temporal Lobe and Right Temporal Lobe are Compared for 3DRP Images and IFBP Images of 15 Iterations with Sieve for an [^{15}O]Water Speech Study

	Size (voxels)	Voxel mean	Centroid (x, y, z)	Average t-value	No. of voxels above t-value threshold for	
					p = 0.01	p = 0.001
LTL 3DRP	80	0.1220	(186, 147, 26)	6.09	80	44
IFBP	113	0.1279	(185, 146, 27)	5.06	113	4
RTL 3DRP	163	0.1287	(76, 140, 27)	6.43	163	115
IFBP	200	0.1325	(77, 140, 27)	5.24	200	27

The two foci were selected based on a 98th percentile threshold of the subtracted 3DRP images. The average t values were calculated from the same voxels used in calculating the voxel mean. The number of voxels presented in the last two columns are those above the 98th percentile and above the two p-value thresholds.
LTL = left temporal lobe; RTL = right temporal lobe.
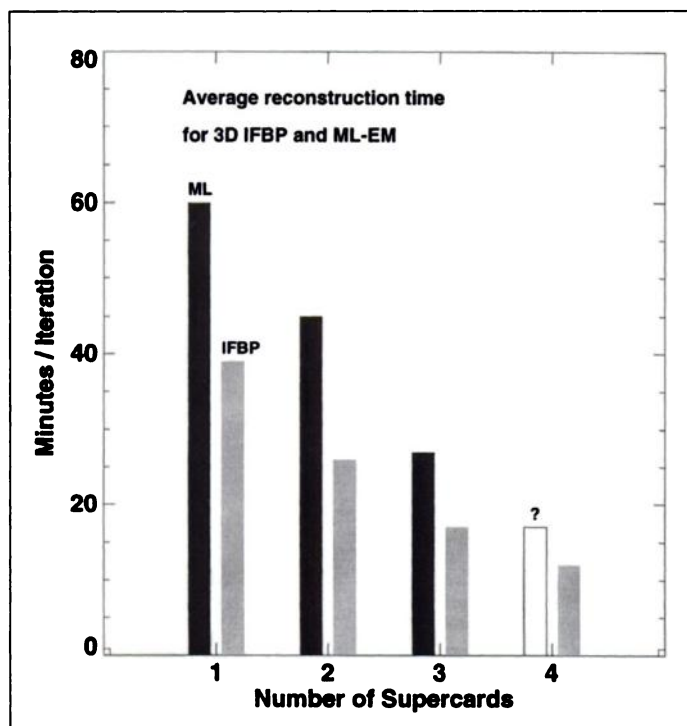
FIGURE 8. Reconstruction time in minutes per iteration for three-dimensional IFBP and ML-EM as a function of the number of supercards. The fourth supercard was not available at the time when the three-dimensional ML-EM was performed.

levels by simply reducing the p-value threshold. Reducing the p value from 0.01–0.001, the number of statistically significant voxels in the IFBP foci dropped further than for 3DRP. Ultimately, statistical thresholds for comparing reconstructions will need to be based on models such as the one proposed in Worsley et al. (28) to compensate for resolution effects and voxel dependency. However, key model assumptions (e.g., t values based on global versus local variance estimates) that will affect such comparisons are still being investigated and debated in the functional neuroimaging community (32,33). In general, because the results we presented are the worst-case scenario, we are optimistic that increased resolution recovery without a significant task-dependent noise increase will be achievable with IFBP.

The Poisson noise model in ML-EM seems to offer some advantage over IFBP in controlling noise in three dimensions (Figs. 4 and 5) as it does in two dimensions. However, 15 iterations for IFBP and 120 iterations for ML-EM do not necessarily represent convergence for the two algorithms, nor should they be considered optimal for resolution matching. Although the mean transaxial resolution for ML-EM is still improving after 120 iterations (Figs. 1C, D), the rate of improvement is negligible. For IFBP, on the other hand, it is possible to introduce a noise model, sophisticated penalty functions or side information to further reduce noise. Therefore, the convergence of three-dimensional ML-EM needs to be studied in greater detail to ensure that its noise performance is compared to that of IFBP at matched image resolution. Other convergence criteria should also be evaluated, and the stopping criteria should be determined by the trade-off between task-dependent signal and noise (bias and variance), especially for different quantitative imaging tasks (29,34).

Our results also indicate that for three-dimensional IFBP and ML-EM, the signal of most visible structures seems to have stabilized by 15 and 120 iterations, respectively—faster than we

previously reported in the two-dimensional case (29), especially for ML-EM. We believe this is due to the different resolution-to-sampling ratios in both images and projections for the two different scanners studied. The ECAT 953B used to generate this dataset has a resolution-to-sampling ratio of <2, whereas the resolution to sampling ratio for the PC4600 (Cyclotron Corp., Berkeley, CA) is >4 (29); the greater this ratio, the slower the convergence. These observations may also explain why different centers using different scanners have reported different optimal stopping criteria for the same iterative algorithms. The effect of intrinsic detector resolution and sampling on the convergence of iterative reconstruction algorithms should be considered in future studies.

Because of the computational burden of three-dimensional algorithms, these studies of two three-dimensional iterative reconstruction algorithms are nontrivial, and their convergence issues, particularly for ML-EM, become very important practically. Further reductions in reconstruction time will depend on how efficiently the three-dimensional forward- and backprojector can be implemented and optimized. With the slow convergence of ML-EM, other speedup tactics such as the space alternative update strategy (19) or ordered subsets (35) should be considered.

CONCLUSION

We have demonstrated that both the three-dimensional IFBP and ML-EM reconstruction algorithms with a resolution model can improve image resolution compared to 3DRP. Examples of phantom, human FDG and [^{15}O]water studies have been presented to support our findings. In general, IFBP achieves resolution improvements with higher noise compared to 3DRP. ML-EM achieves similar resolution improvements compared to 3DRP with almost no noise increase but with a larger iteration number compared to IFBP. The ultimate performance of three-dimensional IFBP and ML-EM should be compared and optimally determined for particular tasks to which they will be applied. To improve reconstruction time, dedicated computer hardware and strategies to speed up the convergence for ML-EM are necessary.

REFERENCES

1. Bailey DL, Jones T, Spinks TJ, Gilardi MC, Townsend DW. Noise equivalent count measurements in a neuro-PET scanner with retractable septa. *IEEE Trans Med Imaging* 1991;10:256–260.
2. Spinks TJ, Jones T, Bailey DL, et al. Physical performance of a positron tomograph for brain imaging with retractable septa. *Phys Med Biol* 1992;37:1637–1655.
3. Cherry SR, Magnus D, Hoffman EJ. Three-dimensional PET using a conventional multislice tomograph without septa. *J Comput Assist Tomogr* 1991;15:655–668.
4. Townsend DW, Spinks TJ, Jones T, et al. Three-dimensional reconstruction of PET data from a multi-ring camera. *IEEE Trans Med Imaging* 1989;36:1056–1065.
5. Kinihan PE, Rogers JG, Harrop R, Johnson RR. Three-dimensional image reconstruction in object space. *IEEE Trans Nucl Sci* 1988;35:635–638.
6. Defrise M, Townsend DW, Clack R. Favor. A fast reconstruction algorithm for volume imaging in PET. *Conference Record of the 1991 IEEE Nuclear Sciences Symposium and Medical Imaging Conference* 1991;3:1919–1923.
7. Daube-Witherspoon ME, Muehllehner G. Treatment of axial data in three-dimensional PET. *J Nucl Med* 1987;28:1717–1724.
8. Lewitt RM, Muehllehner G, Karp JS. Three-dimensional image reconstruction for PET by multi-slice rebinning and axial filtering. *Conference Record of the 1991 IEEE Nuclear Sciences Symposium and Medical Imaging Conference* 1991;3:2054–2061.
9. Defrise M, Sibomana M, Michel C. Three-dimensional PET reconstruction with the ECAT EXACT HR using Fourier rebinning. *Conference Record of the 1995 IEEE Nuclear Sciences Symposium and Medical Imaging Conference*: 1995;3:1316–1320.
10. Kinihan PE, Karp JS. Determining when three-dimensional reconstruction methods are required in volume PET imaging. *Conference Record of the 1992 IEEE Nuclear Sciences Symposium and Medical Imaging Conference* 1992;2:904–906.

11. Medoff BP, Brody WR, Nassi, M, Macovski A. Iterative convolution backprojection algorithms for image reconstruction from limited data. *J Opt Soc Am* 1983;73:1493–1500.
12. Walters TE, Simon W, Chesler DA, Correia JA. Attenuation correction in gamma emission computed tomography. *J Comput Assist Tomogr* 1981;5:9–94.
13. Xu XL, Liow JS, Strother SC. Iterative algebraic reconstruction algorithms for emission computed tomography: a unified framework and its application to positron emission tomography. *Med Phys* 1993;20:1675–1684.
14. Shepp LA, Vardi Y. Maximum likelihood reconstruction for emission tomography. *IEEE Trans Med Imaging* 1982;1:113–122.
15. Lange K, Carson RE. EM reconstruction algorithms for emission and transmission tomography. *J Comput Assist Tomogr* 1984;8:306–316.
16. Liow JS, Strother SC. Noise and signal decoupling in maximum likelihood reconstructions and Metz filter for PET brain images. *Phys Med Biol* 1994;39:735–750.
17. Llacer J, Andreae S, Veklerov E. Towards a practical implementation of the MLE algorithm for positron emission tomography. *IEEE Trans Nucl Sci* 1986;33:468–477.
18. Lalush DS, Tsui BMW. A fast and stable maximum a posterior conjugate gradient reconstruction algorithm. *Med Physics* 1995;22:1273–1284.
19. Sauer K, Bouman C. A local update strategy for iterative reconstruction from projections. *IEEE Trans Signal Proc* 1993;41:534–548.
20. Fessler JA. Penalized weighted least-squares image reconstruction for positron emission tomography. *IEEE Trans Med Imaging* 1994;13:290–300.
21. Mumcuoglu E, Leahy R, Zhou Z, Cherry SR. A phantom study of the quantitative behavior of Bayesian PET reconstruction methods. *Conference Record of the 1995 IEEE Nuclear Sciences Symposium and Medical Imaging Conference:* 1995;3:1703–1707.
22. Lalush DS, Tsui BMW. Improving the convergence of iterative filtered backprojection algorithms. *Med Physics* 1993;21:1283–1286.
23. Clinthorne NH, Pan T-S, Chiao P-C, Rogers WL, Stamos JA. Preconditioning methods for improved convergence rates in iterative reconstructions. *IEEE Trans Med Imaging* 1993;12:78–83.
24. Snyder DL, Miller MI, Thomas LJ Jr, Politte DG. Noise and edge artifacts in maximum-likelihood reconstructions for emission tomography. *IEEE Trans Med Imaging* 1987;6:228–238.
25. Liow JS, Strother SC, Rottenberg DA. Improved resolution via iterative reconstruction for PET volume imaging. *Conference Record of the 1994 IEEE Nuclear Sciences Symposium and Medical Imaging Conference* 1994;3:1315–1319.
26. Palmer BM, Sajjad M, Rottenberg DA. An automated [^{15}O]H$_2$O production and injection system for PET imaging. *Nucl Med Biol* 1995;22:241–249.
27. Woods RP, Mazziotta JC, Cherry SR. MRI-PET registration with automated algorithm. *J Comput Assist Tomogr* 1992;17:536–546.
28. Worsley KJ, Evans AC, Marrett S, Neelin P. A three-dimensional statistical analysis for CBF activation studies in human brain. *J Cereb Blood Flow Metab* 1992;12:900–918.
29. Liow JS, Strother SC. The convergence of object-dependent resolution in maximum likelihood based tomographic image reconstruction. *Phys Med Biol* 1993;38:55–70.
30. Schaper KA, Rehm K, Summers D, et al. Symbolic representation of functional data: the corner-cube environment. *Neuroimage* 1996;3:S166.
31. Snedecor GW, Cochran WG. *Statistical methods.* Ames, IA: Iowa State University Press; 1980.
32. Taylor SF, Minishima S, Koeppe, RA. Instability of localization of cerebral blood flow activation foci with parametric maps. *J Cereb Blood Flow Metab* 1993;13:1040–1041.
33. Worsley KJ, Evans AC, Marrett S, Neelin P. Author's reply. *J Cereb Blood Flow Metab* 1993;13:1041–1042.
34. Carson RE, Yan Y, Chodkowski B, Yap TK, Daube-Witherspoon ME. Precision and accuracy of regional radioactivity quantitation using the maximum likelihood EM reconstruction algorithm. *IEEE Trans Med Imaging* 1994;13:526–537.
35. Hudson HM, Larkin RS. Accelerated image reconstruction using ordered subsets of projection data. *IEEE Trans Med Imaging* 1994;13:601–609.

Fluorine-18-Fluoromisonidazole Radiation Dosimetry in Imaging Studies

Michael M. Graham, Lanell M. Peterson, Jeanne M. Link, Margaret L. Evans, Janet S. Rasey, Wui-Jin Koh, James H. Caldwell and Kenneth A. Krohn

Departments of Radiology and Radiation Oncology, University of Washington School of Medicine; and Division of Cardiology, Department of Medicine, Seattle Veteran's Administration Medical Center, Seattle, Washington

Fluoromisonidazole (FMISO), labeled with the positron emitter ^{18}F, is a useful hypoxia imaging agent for PET studies, with potential applications in patients with tumors, cardiovascular disease and stroke. **Methods:** Radiation doses were calculated in patients undergoing imaging studies to help define the radiation risk of FMISO-PET imaging. Time-dependent concentrations of radioactivity were determined in blood samples and PET images of patients following intravenous injection of [^{18}F]FMISO. Radiation absorbed doses were calculated using the procedures of the Medical Internal Radiation Dose (MIRD) committee, taking into account the variation in dose based on the distribution of activities observed in the individual patients. As part of this study we also calculated an S value for brain to eye. Effective dose equivalent was calculated using ICRP 60 weights. **Results:** Effective dose equivalent was 0.013 mSv/MBq in men and 0.014 mSv/MBq in women. Individual organ doses for women were not different from men. Assuming bladder voiding at 2- or 4-hr intervals, the critical organ that received the highest dose was the urinary bladder wall (0.021 mGy/MBq with 2-hr voiding intervals or 0.029 mGy/MBq with 4-hr voiding intervals). **Conclusion:** The organ doses for [^{18}F]FMISO are comparable to those associated with other commonly performed nuclear medicine tests and indicate that potential radiation risks associated with this study are within generally accepted limits.

Key Words: fluorine-18-fluoromisonidazole; dosimetry; Monte Carlo simulations

J Nucl Med 1997; 38:1631–1636

Fluoromisonidazole ([^{18}F]FMISO, [1-H-1-(3-[^{18}F]fluoro-2-hydroxypropyl)-2-nitroimidazole], RO-07-0741) is a nitroimidazole that is structurally similar to the well-known radiosensitizer, misonidazole. Both molecules distribute throughout the total body water space, readily crossing membranes by passive diffusion. Fluorine-18-FMISO is bound and retained within viable hypoxic cells in an inverse relationship to the oxygen concentration. Binding occurs at the same range of low oxygen levels, which lead to ischemic cellular damage and increased radiation resistance (*1,2*). Fluorine-18-FMISO is currently being used with PET imaging to noninvasively assess hypoxia in human malignancies (*3–6*) and in the hearts of patients with myocardial ischemia (*7*). Accurate radiation dosimetry of [^{18}F]FMISO is required to evaluate the benefits and the relative radiation-related risks. This article presents estimates of the radiation dose to various organs and to the whole body. The estimates are derived from time-activity curves of blood and normal tissue from imaging studies of patients with tumors, coronary artery disease, paralysis or arthritis.

MATERIALS AND METHODS

Patients

Biodistribution data from 60 patients (55 men, 5 women) who underwent [^{18}F]FMISO PET scans at the University of Washington between August 1989 and January 1996 were used for dosimetry estimates. Fifty-four of the individuals had cancer and were imaged to assess tumor hypoxia before radiotherapy, three patients had histories of myocardial ischemia, two were paraplegic and one had rheumatoid arthritis. None of the patients had clinical congestive